NANO LETTERS
Cite This: Nano Lett. 2018, 18, 1660−1667
Letter
pubs.acs.org/NanoLett

Patterns of Carbon Nanotubes by Flow-Directed Deposition on Substrates with Architectured Topographies

M. K. Jawed,*[,†,§] N. G. Hadjiconstantinou,[†] D. M. Parks,[†] and P. M. Reis[†,‡,∥]

[†]Department of Mechanical Engineering and [‡]Department of Civil and Environmental Engineering, Massachusetts Institute of Technology, Cambridge, Massachusetts 02139, United States

[§]Department of Mechanical and Aerospace Engineering, University of California, Los Angeles, Los Angeles, California 90095, United States

[∥]Institute of Mechanical Engineering, École Polytechnique Fédérale de Lausanne, 1015 Lausanne, Switzerland

Supporting Information

ABSTRACT: We develop and perform continuum mechanics simulations of carbon nanotube (CNT) deployment directed by a combination of surface topography and rarefied gas flow. We employ the discrete elastic rods method to model the deposition of CNT as a slender elastic rod that evolves in time under two external forces, namely, van der Waals (vdW) and aerodynamic drag. Our results confirm that this self-assembly process is analogous to a previously studied macroscopic system, the "elastic sewing machine", where an elastic rod deployed onto a moving substrate forms nonlinear patterns. In the case of CNTs, the complex patterns observed on the substrate, such as coils and serpentines, result from an intricate interplay between van der Waals attraction, rarefied aerodynamics, and elastic bending. We systematically sweep through the multidimensional parameter space to quantify the pattern morphology as a function of the relevant material, flow, and geometric parameters. Our findings are in good agreement with available experimental data. Scaling analysis involving the relevant forces helps rationalize our observations.

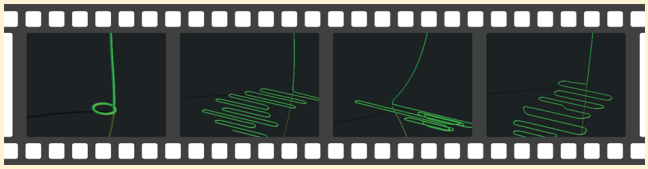

KEYWORDS: *Elastic rod, carbon nanotube, van der Waals, self-assembly, pattern formation, buckling*

Since the discovery of carbon nanotubes (CNTs) a quarter century ago,[1] their unique mechanical, thermal, and electrical properties have found applications in a wide array of nanoelectronic circuits,[2] and energy storage materials,[3] as well as conductive and high-strength composites.[4] Structuring of CNTs along prescribed geometries on surfaces is a prerequisite for functional nanocircuitry and nanodevices.[5] One method to achieve this goal is the controlled deposition of CNT from liquid suspension, which can be accomplished by a variety of techniques including chemically functionalized nanolithographic templates,[6] dispersion in nematic liquid crystals,[7] and dielectrophoresis.[8,9] Alternative approaches to patterned CNTs involve orientation-controlled growth by chemical vapor deposition with the assistance of gas flow, surface structure, or an external field.[10] However, the most successful approach to date for controlling single-wall CNT geometry is nanotube epitaxy (surface-directed growth)[11] combined with external force from rarefied gas flow.[5,12−15] Recent experiments[12−18] have demonstrated remarkable flexibility in setting the geometry of the produced CNT layouts, including serpentine-like shapes and circular patterns. Furthermore, the size and periodicity of these patterns can be tuned by the material and flow parameters. However, a predictive framework that can be used to target and generate patterns of desired size and geometry is notably lacking.

Computationally, molecular dynamics (MD) simulations have been used to simulate the nonlinear mechanical response of CNTs involving large strains and buckling,[19,20] as well as pattern formation.[14,21] However, the computational cost of MD limits the simulation to short time and length scales. This high cost has inspired the development of continuum models for the mechanics of CNT, such as finite element analysis[22−24] and hybrids of continuum and atomistic frameworks.[25]

The aspect ratio (arc-length to radius) of CNTs in self-assembly can be on the order of 10^4−10^5.[12−14] The geometric nonlinearities of the self-assembled patterns and the slenderness of the structure call for an analogy with the theory of Kirchhoff elastic rods.[26] The linear elastic approximation in the mechanics of CNT has been tested in experiments[27] and simulations.[28] Energy scaling analysis, modeling the CNT as an elastic rod, has also provided insight into the size of the serpentines.[29] Still, there is a timely need for a predictive simulation tool that captures the essential physics of the pattern formation process and allows for extensive parameter-space exploration.

Here, we systematically investigate the formation of patterns in CNT using a numerical scheme that adapts the discrete elastic rods (DER)[30] method to include van der Waals (vdW) interactions with the substrate and external aerodynamic

Received: November 4, 2017
Revised: February 16, 2018
Published: February 16, 2018

DOI: 10.1021/acs.nanolett.7b04676
Nano Lett. 2018, 18, 1660−1667

loading. We numerically sweep through parameter space to quantify the pattern morphology as a function of the relevant elastic, geometric, fluid, and vdW parameters. First, the radius of *static coils* (Figure 1a and the Supporting Information, Movie S1) on a planar substrate is numerically quantified, motivated by recent experiments.[14] Subsequently, a substrate with a stepped (staircase-like) topography[12] is introduced, resulting in U-shaped *periodic serpentines* (Figure 1b and the Supporting Information, Movie S2) for a range of flow velocities. For smaller flow velocities, we observe a combination of serpentines and loops; we refer to these as *serpentine-coils* (Figure 1c and the Supporting Information, Movie S3). For flow velocities above a threshold value, *irregular serpentines* form (Figure 1d and the Supporting Information, Movie S4). We pay particular attention to periodic serpentine patterns and quantify their amplitude and wavelength. We also explore the formation of serpentines as a function of flow direction. A scaling analysis involving elastic, vdW, and aerodynamic forces determines the dimensionless groups that dictate the size of these patterns. Finally, we establish analogies between the current microscopic system and other related problems where a filamentary structure impacts a rigid substrate to form periodic patterns, such as deployment of an elastic rod[31−34] or a viscous filament[35] onto a moving substrate, direct writing of micro-structured fibers,[36] and manufacturing of spun-bonded non-woven fabrics.[37]

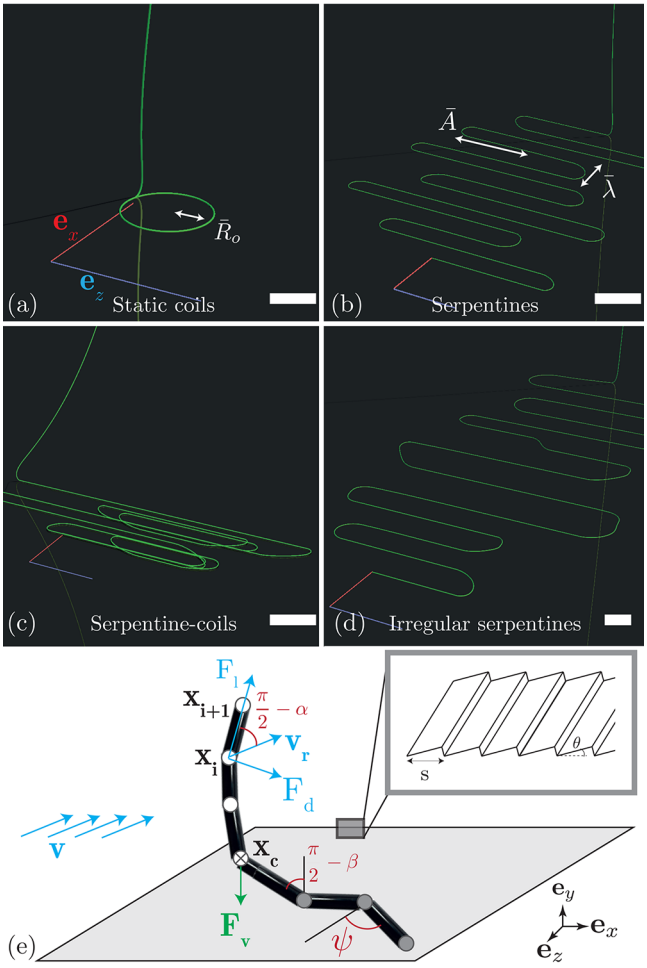

Figure 1. ((a) Static coiling on a substrate. (b) Periodic serpentines, (c) serpentine-coils, and (d) irregular serpentines can form when the substrate has a stepped topography. All the parameters correspond to the baseline cases at different normalized velocities. Scale bar: 2 μm. The rod radius is scaled ×10 for visualization purposes. (e) Discretization and relevant parameters. Inset: a stepped substrate is necessary to generate serpentines.

Problem Statement and DER Simulations. We model the CNT as a Kirchhoff elastic rod,[26] from hereon referred to simply as *rod*. Figure 1e shows a schematic diagram and associated discretization of our problem. The substrate lies along the x−z plane, and at time $t = 0$, the rod of length H is positioned perpendicularly to the substrate. Within the discrete setting of the DER computational framework (discussed in Section S3 of the Supporting Information), the rod is discretized along its arc-length into N nodes with coordinates, $\mathbf{x}_i$ $(0 \le i < N)$. An orthonormal material frame that is aligned with the tangent, $\mathbf{t}_i = \mathbf{e}_i/|\mathbf{e}_i|$, is associated with each edge, $\mathbf{e}_i = \mathbf{x}_{i+1} - \mathbf{x}_i$, and its orientation with respect to the reference frame (also aligned with the tangent) is represented by θ_i with $0 \le i < N - 1$. Elastic energies (bending, twisting, and stretching) are derived in terms of $\mathbf{x}_i$ and θ_i, representing a total of $4N - 1$ scalar variables. Discrete versions of the $4N - 1$ equations of motion are derived by obtaining the gradient of the elastic energies (i.e., forces on $\mathbf{x}_i$ and moments on θ_i), and equating them to the balance of inertial and external (van der Waals and aerodynamic) forces.

As nodes are deposited onto the substrate, additional nodes are injected at the free end of the rod (and, therefore, N increases with time) to keep the height, H, fixed at the prescribed value. For computational efficiency, all the deposited nodes far beyond the point of contact with the substrate are deleted from the simulation. In our simulations, we use a distance of 25 μm (measured along the arc-length) from the contact point as a condition for node deletion (more details in the Supporting Information, Section S3).

Our starting point was an existing DER code[38] that was previously validated against experiments.[32] We now detail the modifications required to include the external forces and boundary conditions of the current system.

van der Waals Interactions. The vdW energy between the CNT and the substrate can be computed from a Lennard-Jones potential.[29,39] Without loss of generality, we choose the coordinate system such that $y = 0$ corresponds to the minimum of this energy landscape. This vdW energy becomes negligible for $y \gtrsim 10^{-3}$ μm, while the height of the CNT reported in experiments is $H \approx 10^2$ μm.[12,14] Given this separation of length scales, we took the edge length of the discrete rod, $\delta = |\mathbf{e}_i|$, to be between these two values: 10^{-3} μm $\ll \delta \ll H$. The vdW force can then be compared with an adhesive force that acts only close to the contact point. A convergence study for this discretization length, δ, has been performed (Section S4, Supporting Information).

In order to model the contact between the rod and the substrate, when a node penetrates the $y = 0$ plane, it is considered *deposited* (represented by the filled circles in Figure 1e) and is then constrained vertically (y-coordinate is fixed at 0) for the remainder of the simulation. The vdW force, $\mathbf{F}_v$, acts only on the $\mathbf{x}_c$ node (indicated by a cross in Figure 1e), above the contact point, $\mathbf{x}_{c-1}$. The vdW potential energy per length, e_v, of the contact edge $\mathbf{x}_c - \mathbf{x}_{c-1}$ can be evaluated numerically from the Lennard-Jones potential between two carbon atoms. Physically, e_v is the required energy per unit length to move a CNT from $y = 0$ (oriented parallel to the substrate) to $y = \infty$. In order to simplify the calculation, we take the total vdW

DOI: 10.1021/acs.nanolett.7b04676
Nano Lett. 2018, 18, 1660−1667

energy of the contact edge, E_v, to vary linearly with the contact angle, β (angle between the contact edge and the substrate), namely, $E_v = \frac{e_v\delta}{\beta_0}(\beta - \beta_0)$, where β_0 is the angle between the edge $\mathbf{x}_c - \mathbf{x}_{c-1}$ and the substrate (x–z plane) when the node $\mathbf{x}_{c-1}$ touched the substrate. The details of this linearization are provided in Section S1 of the Supporting Information. The corresponding vdW force on $\mathbf{x}_c$ is

$$\mathbf{F}_v = -\frac{\partial E_v}{\partial \beta}\frac{\partial \beta}{\partial \delta_y}\hat{\mathbf{e}}_y = -\frac{e_v\delta}{\beta_0}\frac{1}{\sqrt{\delta^2 - \delta_y^2}}\hat{\mathbf{e}}_y \quad (1)$$

where $\delta_y = \hat{\mathbf{e}}_y\cdot(\mathbf{x}_c - \mathbf{x}_{c-1})$ is the projection of the edge of the discrete rod at the contact point on the substrate.

Aerodynamic Loading from the Rarefied Gas Flow. The aerodynamics of the gas flow in CNT self-assembly is in the rarefied regime since the mean free path of the gas is significantly larger than the tube radius.[40] A force model consistent with the rarefied nature of the flow is discussed next. Each edge in the discrete rod is essentially a cylinder with radius, r_0, length, δ, and velocity, $\dot{\mathbf{x}}_i$. In Section S2 of the Supporting Information, we consider a cylinder moving with velocity $\dot{\mathbf{x}}_i$ through a rarefied flow of velocity $\mathbf{v}$. If the angle between the cylinder axis and the relative velocity, $\mathbf{v}_r = \mathbf{v} - \dot{\mathbf{x}}_i$, is $\pi/2 - \alpha$ (see Figure 1e), the aerodynamic force per unit length is

$$\mathbf{F}_a = \sigma\mu \sin\alpha(\mathbf{v}_r\cdot\mathbf{t})\mathbf{t} + C_\sigma\mu\cos\alpha(\mathbb{I} - \mathbf{t}\otimes\mathbf{t})\mathbf{v}_r \quad (2)$$

where the coefficients μ and C_σ are described next. The effective viscosity parameter μ resembles the dynamic viscosity of continuum low Reynolds flow (also with units of [Pa s]), and depends on the density of the gas, ρ_∞, and the radius of the CNT, r_0, namely, $\mu = v_0\rho_\infty r_0$, where $v_0 = 1345$ ms^{-1} is evaluated based on the composition of the gas mixture. The numerical prefactor C_σ in eq 2 depends on the probability of diffuse reflection, σ, of the CNT surface. For $\sigma = 0$, all the gas molecules impinging on a surface are reflected specularly, whereas $\sigma = 1$ corresponds to completely diffuse reflection. The value of C_σ varies from 2.0 to 2.29, as σ changes from 0 to 1. Given the relatively small variation (14%) in C_σ with σ, hereon, we use $\sigma = 1$ and $C_\sigma = 2.29$, and leave a more detailed study on the nature of the CNT surface for future work. We also note that diffuse reflection ($\sigma = 1$) is an often-used assumption for engineering (rough) surfaces.[41]

Physical Parameters for Baseline System. Guided by the experiments reported in refs 12 and 14, we focus our attention in the baseline case of a CNT with radius $r_0 = 1.356$ nm corresponding to a chiral index of (20,20)[42] and height $H = 20$ μm. The resulting vdW potential value $e_v = 4.39 \times 10^{-10}$ J/m (corresponding to a planar graphite substrate) is calculated using the methodology of ref 29 outlined in Section S1.1 of the Supporting Information. For a stepped substrate with a step width $s = 3$ nm and slope angle $\theta = 0.22$ rad (see Figure 1e), the potential is estimated to be $e_v = 1.64 \times 10^{-10}$ J/m (see Section S1.2 of the Supporting Information). The mass per unit length of the CNT is $\rho = 8.1 \times 10^{-15}$ kg/m.[43] The effective viscosity for a rarefied gas medium with density $\rho_\infty = 0.28$ kg/m^3 is $\mu = 5.11 \times 10^{-7}$ Pa s.

We now turn to the elastic properties of the CNT. The bending stiffness can be evaluated from $k_b = \pi C r_0^3$. The in-plane stiffness was taken as $C = 345$ J/m^2 from *ab initio* computation[44,45] yielding $k_b = 2.7 \times 10^{-24}$ N m^2, which will serve as our baseline case. We approximate the twisting stiffness, k_t, to be equal to the bending stiffness, k_b;[28] no variation in pattern morphology was observed as k_t/k_b was varied between 0.1 and 10. The stretching stiffness of $k_s = 2.9 \times 10^{-6}$ N can be estimated from $k_s = 2Y\pi t r_0$,[46,47] with $Y = 1$ TPa for the Young's modulus, and $t = 0.34$ nm for the effective tube thickness (interlayer spacing of graphite). As the prominent mode of deformation is bending, the CNT dynamics has negligible dependence on k_s (Section S5, Supporting Information). A detailed discussion on the axial stiffness of CNT can be found in ref 48. Throughout our study, twisting and stretching stiffness values are chosen such that the dimensionless groups, k_t/k_b and k_s/e_v, remain fixed in their baseline case ($k_t/k_b = 1$; $k_s/e_v = \{6.6 \times 10^3, 1.8 \times 10^4\}$ for planar and stepped substrates, respectively).

We model the slender CNT as an elastic rod and develop vdW and aerodynamic force models based on Lennard-Jones potential and molecular momentum transfer so that we can use a discretization length much larger than a nanometer. As a result, in scenarios involving distortion of cross-sectional shape of CNT, e.g., kink formation[19] and radial deformation of CNT on substrate,[22] the elastic rod model is inadequate (Section S7, Supporting Information). In what follows, we explore the pattern formation process and quantify the associated characteristic length scales, as a function of the following physical parameters: height of rod (H), CNT mass per unit length (ρ), bending stiffness (k_b), vdW potential between the CNT and the substrate (e_v), and effective viscosity of the rarefied gas flow (μ).

Static Coiling. Before studying more complex patterns, we first consider the deposition of a CNT on a substrate without a freestream velocity. Shadmi et al.[14] first investigated this scenario experimentally, accompanied by molecular dynamics simulations. We ignore the self-interaction of CNT—when the falling CNT and its already deposited portions come in contact, they may reorient due to vdW forces.[14] We leave the extension of the simulations to account for this interaction to future study.

We note that the vdW forces from a perfectly planar substrate do not resist motion in the x–z plane. Indeed, in our simulations, we find that coils do not form on such a perfect substrate. On the other hand, we expect that imperfections will invariably be present in any experiment. For example, already deposited portions of a rod increase the roughness of the substrate and impede motion. To model such imperfections, all three degrees of freedom of a node are fixed upon contact with the substrate. Furthermore, near the contact point, the rod is initialized in the curved configuration shown in Figure 2a with radius of curvature $R_i \approx 0.5$ μm $\ll H$. This induced imperfection is sufficient for the vdW interaction to self-initiate deployment. As shown in Section S6 of the Supporting Information, the pattern size does not depend on R_i.

In Figure 2, we present a time-series of snapshots of the coil formation process in our baseline case. After an initial transient regime (Figure 2a–c) that lasts $\approx 2 \times 10^{-6}$ s, the rod forms circular coils with a radius of $R_0 = 0.60 \pm 0.01$ μm (Figure 2d). For generality, we now seek a dimensionless description of the coiling radius and the physical parameters. Balancing the bending and the vdW forces[45] yields the characteristic *vdW-bending length*,

$$L_{vb} = \sqrt{\frac{k_b}{e_v}} \quad (3)$$

DOI: 10.1021/acs.nanolett.7b04676
Nano Lett. 2018, 18, 1660–1667

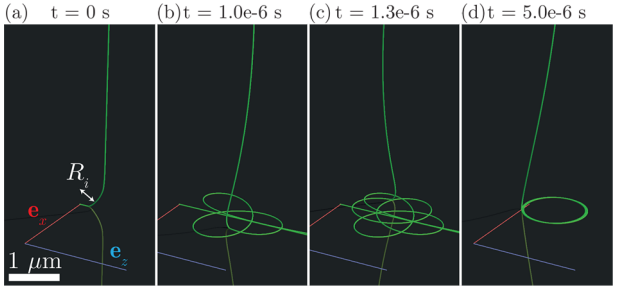

Figure 2. Snapshots from our simulation showing the formation of static coils of the CNT (Supporting Information, Movie S1) at (a) t = 0 s, (b) $t = 1.0 \times 10^{-6}$ s, (c) $t = 1.3 \times 10^{-6}$ s, and (d) $t = 5.0 \times 10^{-6}$ s. The physical parameters correspond to the baseline setup. Deposited portion of the CNT beyond 100 nm from the contact point is not shown in the visualization.

This characteristic length scale sets the curvature of the rod near the contact point. The parameters of the baseline case yield L_{vb} = 0.078 μm. Note that L_{vb} is analogous to the *gravito-bending length* (arising from the balance between gravity and bending forces), which was found to govern the periodicity and size of the patterns observed in the macroscopic system of a falling elastic rod on a moving belt, also known as the elastic sewing machine.[32,33] Hereafter, an overbar denotes a non-dimensional quantity (i.e., quantities with units of length are normalized by L_{vb}); e.g., $\bar{H} = H/L_{vb}$. Given the number of parameters in this problem, namely, $\{R_0, H, e_v, \rho, \mu, k_b\}$, we can write

$$\bar{R}_0 = \hat{R}_0(\bar{H}, \bar{I}) \tag{4}$$

where $\bar{I} = \frac{\rho e_v^2}{k_b \mu^2}$ can be interpreted as the dimensionless inertia.

We proceed by obtaining numerical data to characterize the relation in eq 4 and thus obtain the functional dependence of the coiling radius, R_0, on the relevant physical parameters. In Figure 3a, having fixed $\bar{H}$ = 253 and $\bar{I}$ = 2200 (baseline values), we plot the normalized coiling radius, $\bar{R}_0$, as a function of L_{vb}. We vary L_{vb} by changing one of the two parameters (bending stiffness in the range $2.7 \times 10^{-25} \leq k_b$ [N m^2] $\leq 2.7 \times 10^{-23}$ and the vdW potential in the range $4.39 \times 10^{-11} \leq e_v$ [J/m] $\leq 4.39 \times 10^{-9}$ J/m), and keep the second one fixed at its baseline value. As the value of k_b (or e_v) is varied, the height, H, and mass per length, ρ, are scaled appropriately so that the dimensionless groups $\bar{H}$ and $\bar{I}$ remain constant. We find that, regardless of the value of L_{vb}, the normalized coiling radius remains constant at $\bar{R}_0 = 7.64 \pm 0.01$, and thus confirms the nondimensionalization scheme introduced in eq 4.

Next, we perform a series of simulations to investigate the variation in the coiling radius with height within the experimentally relevant range ($10^2 < \bar{H} < 10^4$), and keep all the other parameters fixed at the baseline values. In Figure 3b, we plot $\bar{R}_0$ versus $\bar{H}$, for $\bar{I}$ = 2200 (baseline value). All the data beyond a threshold height ($\bar{H} \gtrsim 200$) is found to collapse onto a curve that is consistent with a power-law

$$\bar{R}_0 = a\bar{H}^{\gamma} \tag{5}$$

where $a = 2.5 \pm 0.4$ and $\gamma = 0.21 \pm 0.02$ are numerical constants obtained by fitting the data.

Similarly to the procedure followed to obtain the data in Figure 3b, we also perform a parameter sweep and independently vary the mass per length, ρ, and the effective viscosity, μ, while keeping the remaining nondimensional

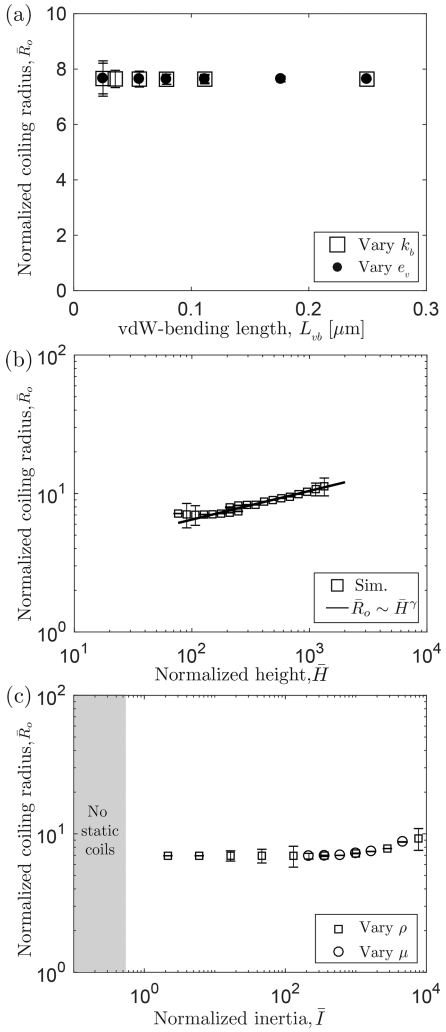

Figure 3. (a) Normalized coiling radius, $\bar{R}_0$, as a function of vdW-bending length, L_{vb}, at $\bar{H}$ = 253 and the dimensionless inertia $\bar{I}$ = 2200. (b) Normalized coiling radius, $\bar{R}_0$, vs normalized height, $\bar{H}$, at $\rho e_v^2/[k_b \mu^2]$ = 2200. (c) Normalized coiling radius, $\bar{R}_0$, versus $\bar{I}$, at $\bar{H}$ = 253.

parameters fixed such that $\bar{H}$ = 253. Figure 3c shows the relation between $\bar{R}_0$ and the dimensionless inertia $\bar{I}$, for $\bar{H}$ = 253. We observe that, when $1 \lesssim \bar{I} \lesssim 10^3$, the coiling radius remains nearly constant. As $\bar{I}$ increases beyond 10^3, and inertial effects become important, $\bar{R}_0$ only exhibits a moderate increase ($\bar{R}_0$ increases by 35% as $\bar{I}$ increases from 2×10^2 to 8×10^3). Furthermore, when $\bar{I} \lesssim 1$, the deposited CNT patterns are irregular, instead of circular coils described above. This can be attributed to the role of the aerodynamic drag on the formation of coils: as $\bar{I}$ decreases, the resistance to motion due to drag is reduced, and beyond a threshold, the drag becomes inadequate to hold the growing CNT in place to form coils.

Overall, the coiling radius is well-described by the empirical relation in eq 5, over a wide range of the parameter space ($\bar{H} \gtrsim 10^2$ and $1 \lesssim \bar{I} \lesssim 10^4$) that encompasses the parameter range relevant to recent experiments.[14] The coiling radii plotted in Figure 3a–c vary between 0.5 and 1.0 μm. Shadmi et al.[14] reported experimental coiling radii in the range 0.5–5 μm, in remarkable agreement with our simulations, with no adjustable parameters. At present, a more direct comparison with experimental results is not feasible due to a lack of published

DOI: 10.1021/acs.nanolett.7b04676
Nano Lett. 2018, 18, 1660–1667

precise experimental data in the literature for the elastic moduli of CNTs, as well as the other physical parameters: H, μ, r_0, e_v.

Serpentine Patterns. Thus far, we have considered a quiescent rarefied gas medium and a perfectly sticky substrate. Motivated by experiments reported by Geblinger et al.,[12] we now expand our model system to include the following: (i) a freestream velocity of the gas, $v\hat{\mathbf{e}}_x$, along the x-axis (perpendicular to the steps), and (ii) a staircase-like substrate with a step-size, s, defined as the distance between two subsequent ridges (inset of Figure 1e), in lieu of a sticky planar substrate used for static coiling. Since the topography does not vary along the z-axis, the rod may slide after deposition on the substrate (details are provided in Sections S1 and S3 of the Supporting Information). Such sliding dynamics were also observed in the molecular dynamics simulations of serpentine formation by CNT.[21] The two new parameters, v and s, call for two additional dimensionless groups: the normalized flow velocity, $\overline{v} = v\mu H/e_v$, and the normalized step-size, $\overline{s} = s/L_{vb}$, where the vdW-bending length is $L_{vb} = 0.13$ μm. For the baseline case, we take $s = 3$ nm (i.e., $\overline{s} = 0.023$),[21] and vary the dimensionless flow velocity in the range $0 \leq \overline{v} \leq 0.13$, which is treated as the primary control parameter.

Prior to reporting our numerical results for the serpentine patterns, we describe the numerical scheme employed to include the stepped substrate (details in Section S1.2 of the Supporting Information). We first note the separation of length scales, $s \ll L_{vb} \ll H$ and our choice of discretization length $\delta \sim L_{vb}$ (Section S4, Supporting Information). Since the substrate corrugation length scale, quantified by s, is negligible compared to the discretization length, the rod is, effectively, deposited on a flat substrate at $y = 0$. Once a node of the rod has been deposited and its y-coordinate fixed at $y = 0$, we examine the effect of the corrugation only on the deposited nodes. As detailed in Section S1.2 of the Supporting Information, we invoke the concept of *critical curvature*, κ_c,[32] and summarize it next. The curvature between a deposited edge, $\mathbf{e}_i$, and the z-axis, $\hat{\mathbf{e}}_z$ (parallel to the steps), is $2\tan(\psi/2)/\delta$ where δ is the edge length, and ψ is the angle between $\mathbf{e}_i$ and $\hat{\mathbf{e}}_z$ such that $\tan\psi = (\mathbf{e}_i\cdot\hat{\mathbf{e}}_x)/(\mathbf{e}_i\cdot\hat{\mathbf{e}}_z)$ (see Figure 1e for a schematic of ψ).[49] If this curvature falls below a critical value, κ_c, such that $2\tan(\psi/2) < \kappa_c\delta$, then the edge reorients along the step direction (z-axis). Since $\kappa_c\delta \ll 1$ throughout our study, we can simplify this condition to $(\mathbf{e}_i\cdot\hat{\mathbf{e}}_x)/(\mathbf{e}_i\cdot\hat{\mathbf{e}}_z) < \kappa_c\delta$. In the baseline case, the normalized critical curvature is $\overline{\kappa}_c := \kappa_c L_{vb} = 0.2$. Even though using a threshold curvature is a simplification, our results below show that the amplitude and periodicity of the pattern are not sensitive to the choice of κ_c.

We now explore the phase boundaries for the various types of observed patterns, as well as the amplitude and wavelength of the serpentines (see Figure 1), as functions of the four dimensionless groups: $\{\overline{\kappa}_c, \overline{v}, \overline{H}, \overline{I}\}$. In Figure 4a, we construct a phase diagram on $(\overline{\kappa}_c, \overline{v})$, with the other two groups fixed at their baseline values for the stepped substrate: $\overline{H} = 155$ and $\overline{I} = 300$. We vary $\overline{\kappa}_c$ and $\overline{v}$ by individually varying κ_c and v, respectively, while fixing all other parameters. In Figure 4a, we observe that, at a fixed value of $\overline{\kappa}_c$, serpentine-coils (Figure 1c) form at lower values of normalized velocity, $\overline{v}$. Past a threshold of the flow velocity, periodic serpentines (Figure 1b) emerge. Irregular serpentines (Figure 1d) are then observed past a second threshold. It is interesting to note that, for $0.1 \lesssim \overline{\kappa}_c \lesssim 0.15$, periodic serpentines appear over a wide range of $\overline{v}$. This points to the importance of substrate choice and the physical properties of CNT for optimal generation of periodic serpentine patterns.

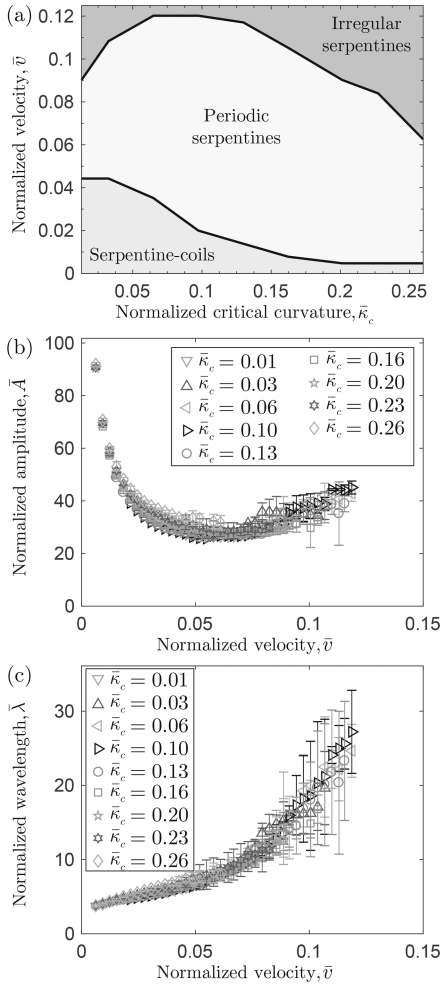

Figure 4. (a) Phase diagram on $(\overline{v},\overline{\kappa}_c)$, with the colors corresponding to different patterns. (b) Normalized amplitude, $\overline{A}$, vs normalized velocity, $\overline{v}$, at different values of normalized critical curvature, $\overline{\kappa}_c$. The dimensionless groups, $\{\overline{H}, \overline{I}\}$, were fixed at the baseline case. (c) Normalized wavelength, $\overline{\lambda}$, from the same data.

In Figure 4b, we plot the normalized amplitude, $\overline{A}$, versus the normalized velocity, $\overline{v}$, at different values of $\overline{\kappa}_c$. All the data collapses onto a single curve, even though the region of stability of serpentine varies with $\overline{\kappa}_c$. For example, as the velocity increases from $\overline{v} \approx 0$ to $\overline{v} \approx 0.07$, the amplitude decreases from $\overline{A} \approx 100$ to $\overline{A} \approx 25$. Beyond $\overline{v} \approx 0.07$, there is a slight increase in $\overline{A}$. In Figure 4c, we present a plot of the normalized wavelength of the serpentines, $\overline{\lambda}$, versus $\overline{v}$. Again, we find the data follows a master curve, with $\overline{\lambda}$ increasing from $\overline{\lambda} \approx 4$ to $\overline{\lambda} \approx 25$.

Overall, the above results offer a rich design space for microfabrication applications with approximately 400% variation in amplitude and wavelength. The amplitude and wavelength of the serpentines in the baseline case vary in the ranges $3 \lesssim A\ [\mu\text{m}] \lesssim 13$ and $0.5 \lesssim \lambda\ [\mu\text{m}] \lesssim 3$. These results are consistent with the serpentine shapes measured experimentally by Geblinger et al.[12] Moreover, the agreement between our simulations and experiments provides further support for the validity of our computational framework.

We now turn to exploring the remaining two dimensionless groups, normalized height, $\overline{H}$, and dimensionless inertia, $\overline{I}$, and

DOI: 10.1021/acs.nanolett.7b04676
Nano Lett. 2018, 18, 1660−1667

fix the freestream velocity at $\bar{v}$ = 0.037 and $\bar{\kappa}_c$ = 0.2 (baseline values). In Figure 5a, we plot the amplitude and wavelength as

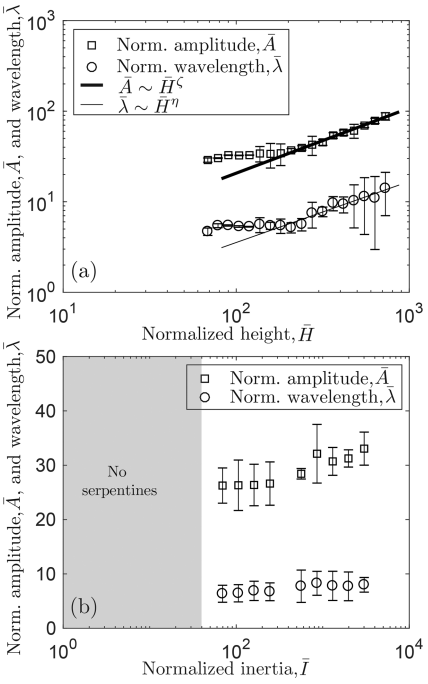

Figure 5. (a) Normalized amplitude, $\bar{A}$, and wavelength, $\bar{\lambda}$, as a function of normalized height, $\bar{H}$, while keeping all other dimensionless groups fixed at their baseline values. The solid lines show the fit to $\bar{A} \sim \bar{H}^{\zeta}$ (ζ = 0.72 ± 0.06) and $\bar{\lambda} \sim \bar{H}^{\eta}$ (η = 0.67 ± 0.16) for $\bar{H}$ > 200. (b) $\bar{A}$ and $\bar{\lambda}$ vs the dimensionless inertia, $\bar{I}$. All the parameters except the mass per length, ρ, remained at the baseline case value.

a function of the normalized height, $\bar{H}$, at $\bar{I}$ = 300. In our scheme for parameter-space exploration, we vary the height, H, while also scaling the velocity, v (and viscosity, μ), to keep the dimensionless group $\bar{v}$ (and $\bar{I}$) constant. All other physical parameters are fixed at their baseline values. The range of height explored here ($70 \lesssim \bar{H} \lesssim 700$, i.e., 8 μm $\lesssim$ H $\lesssim$ 100 μm) was chosen to contain the range over which experimental data is available.[12,14] As shown by solid lines in Figure 5a, we find that, for $\bar{H} \gtrsim 200$, the amplitude (wavelength) scales reasonably well as $\bar{A} \sim \bar{H}^{\zeta}$ ($\bar{\lambda} \sim \bar{H}^{\eta}$), where ζ = 0.72 ± 0.06 (η = 0.67 ± 0.16) is a numerical constant evaluated by fitting the data.

The similar functional dependence of $\bar{R}_0$ for static coiling in eq 5 and the empirical relation proposed for $\bar{A}$ (or $\bar{\lambda}$) in serpentines reaffirm the connection of CNT self-assembly with the analogous macroscopic systems of elastic[32] and fluid-mechanical[35] sewing machines. The main commonality across all three systems (the two macroscopic cases and the CNT deployment problem) is the prominence of an *intrinsic* length scale set by the physical ingredients.[34,50] Specifically, in the elastic sewing machine this length scale arises from a combination of the elastic moduli and gravity, and in the fluid-mechanical sewing machine it relates to a balance between viscosity and gravity. As the elastic rod or viscous thread buckles due to contact with the substrate, this length scale is excited, thereby setting the shape of the patterns. Similarly, in the present study, the CNT patterns are set primarily by the vdW-bending length, L_{vb}.

In Figure 5b, we plot the amplitude and wavelength versus dimensionless inertia, $\bar{I}$, at $\bar{H}$ = 155 (the other two dimensionless parameters, $\bar{v}$ and $\bar{\kappa}_c$, were fixed at their baseline values). To vary $\bar{I}$, we varied the mass per length, ρ, while fixing the other parameters. The change in the size of the serpentines is relatively small (the amplitude remains in the range $26 < \bar{A} < 33$ and $6.3 < \bar{\lambda} < 8.3$ for the wavelength) even though $\bar{I}$ is varied over 2 orders of magnitude.

Finally, motivated by recent experimental observations,[12] we probe the effect of the direction of the freestream flow velocity, with respect to the steps on the substrate, on serpentine formation (Figure 6a1,a2). Up to this point, the flow velocity

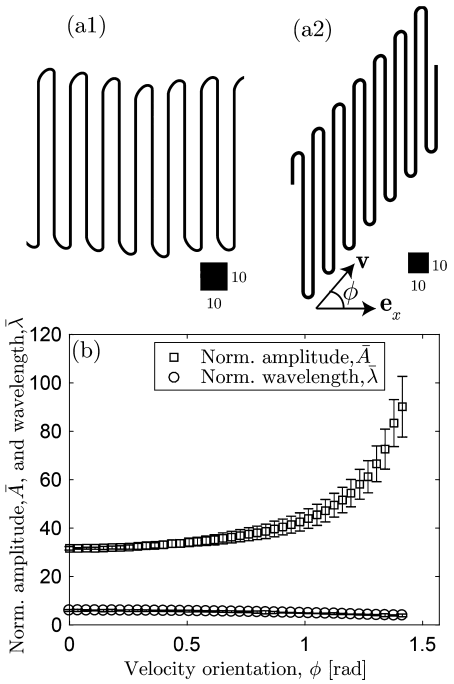

Figure 6. (a) Trace of the patterns on x–z plane [normalized by L_{vb}] at (a1) ϕ = 0 rad, (a2) ϕ = 0.87 rad. (b) Normalized amplitude, $\bar{A}$, and wavelength, $\bar{\lambda}$, vs the orientation of the freestream velocity, ϕ. The norm of the velocity was $\bar{v}$ = 0.037, and all the physical parameters were held fixed at the baseline case.

was imposed perpendicularly to the steps on the substrate, such that the angle between $\mathbf{v}$ and $\hat{\mathbf{e}}_x$ was ϕ = 0. Now, we fix the norm of the velocity at $\bar{v}$ = 0.037 (and the dimensionless groups at their baseline values), and vary its orientation, ϕ, relative to the x-axis. Figure 6a1,a2 presents examples of patterns at two different orientations: ϕ = {0.0, 0.87} rad, respectively. When the orientation angle is zero (e.g., Figure 6a1), regular serpentines form along the x-axis. At higher values of ϕ (e.g., Figure 6a2), skewed serpentines form along the direction of $\mathbf{v}$. Both of these findings are well-aligned with the recent experiments described by Geblinger et al.[12] At sufficiently high values of ϕ, close to $\pi/2$ rad, the misalignment between the x-axis and the imposed flow velocity inhibits formation of periodic serpentines. In order to quantify the effect of ϕ, in Figure 6b, we plot the amplitude and wavelength as functions of ϕ. Both amplitude and wavelength vary nonlinearly as functions of ϕ. As ϕ increases from 0 to $\pi/2$, the amplitude increases from $\bar{A}$ = 32 to $\bar{A}$ = 90 while the wavelength decreases from $\bar{\lambda}$ = 6.0 to $\bar{\lambda}$ = 3.9. This indicates the potential of using the flow orientation as a means to tune the serpentine morphology.

Discussion and Conclusions. We have introduced a physically based continuum simulation of CNT self-assembly

DOI: 10.1021/acs.nanolett.7b04676
Nano Lett. 2018, 18, 1660−1667

under combined surface- and flow-directed growth. Our results provide a succinct description of the radius of the coils and the wavelength and amplitude of the serpentines, across a wide range of parameter space of engineering relevance to experiments. The prediction of pattern morphology from our simulations can potentially be used to target and design patterns with a desired geometry.

The relatively small computational cost of our numerical framework may be leveraged to run our simulation in conjunction with an optimization scheme tfor laying down CNTs along a circuit diagram. Given that the electrical properties (e.g., conductance) vary with the bending radius in serpentines,[51] our framework can be used to tune such properties. We hope that our results will inspire further experimental work to characterize the physical parameters of the system, e.g., elastic stiffness, probability of diffuse reflection, and substrate topography.

More broadly, our analysis extends a remarkable connection[12,19] between microscopic CNT self-assembly and the elastic sewing machine, as well as several other macroscopic systems where a filamentary structure is deployed onto a moving substrate. In the current case of pattern formation in CNTs, an intrinsic length arises from the balance between bending and vdW forces. Ultimately, this characteristic length sets the size of all the patterns quantified by the radius of a circular coil, as well as the wavelength or amplitude of serpentines. Depending on the physical ingredients and the constitutive description of the filament, this intrinsic length varies but the underlying geometric description is common across all of these systems, ranging from macroscopic viscous thread on a moving belt to the microscopic patterns in CNTs.[34,52] We expect that the knowledge gained from these relatively well-studied macroscopic systems of a falling viscous thread or elastic rod on a moving belt can further advance our understanding of the coiling patterns in CNTs.

■ ASSOCIATED CONTENT

Supporting Information

The Supporting Information is available free of charge on the ACS Publications website at DOI: 10.1021/acs.nanolett.7b04676.

Details of external force (van der Waals and rarefied aerodynamics) implementation, DER simulation procedure, convergence study on the discretization length, sensitivity study on stretching stiffness, and sensitivity study on imperfection curvature (PDF)

Movie S1, simulation of static coiling for the baseline case with $\bar{H}$ = 252, $\bar{I}$ = 2200; Movie S2, simulation of serpentine formation with $\bar{v}$ = 0.69, $\bar{\kappa}_c$ = 0.2, $\bar{H}$ = 155, $\bar{I}$ = 300; Movie S3, simulation of serpentine-coil formation with $\bar{v}$ = 0.019, $\bar{\kappa}_c$ = 0.2, $\bar{H}$ = 155, $\bar{I}$ = 300; and Movie S4, simulation of irregular serpentine formation with $\bar{v}$ = 0.12, $\bar{\kappa}_c$ = 0.2, $\bar{H}$ = 155, $\bar{I}$ = 300 (ZIP)

■ AUTHOR INFORMATION

Corresponding Author

*E-mail: khalidjm@seas.ucla.edu.

ORCID

M. K. Jawed: 0000-0003-4661-1408

Notes

The authors declare no competing financial interest.

■ ACKNOWLEDGMENTS

We are grateful for financial support from the National Science Foundation (CMMI-1129894).

■ REFERENCES

(1) Iijima, S. *Nature* **1991**, *354*, 56−58.
(2) Wei, B.; Vajtai, R.; Ajayan, P. *Appl. Phys. Lett.* **2001**, *79*, 1172−1174.
(3) Frackowiak, E.; Beguin, F. *Carbon* **2001**, *39*, 937−950.
(4) Baughman, R. H.; Zakhidov, A. A.; de Heer, W. A. *Science* **2002**, *297*, 787−792.
(5) Joselevich, E. *Nano Res.* **2009**, *2*, 743−754.
(6) Liu, J.; Casavant, M. J.; Cox, M.; Walters, D.; Boul, P.; Lu, W.; Rimberg, A.; Smith, K.; Colbert, D. T.; Smalley, R. E. *Chem. Phys. Lett.* **1999**, *303*, 125−129.
(7) Lynch, M. D.; Patrick, D. L. *Nano Lett.* **2002**, *2*, 1197−1201.
(8) Krupke, R.; Hennrich, F.; Löhneysen, H. v.; Kappes, M. M. *Science* **2003**, *301*, 344−347.
(9) Diehl, M. R.; Yaliraki, S. N.; Beckman, R. A.; Barahona, M.; Heath, J. R. *Angew. Chem., Int. Ed.* **2002**, *41*, 353−356.
(10) Chen, Y.; Zhang, Y.; Hu, Y.; Kang, L.; Zhang, S.; Xie, H.; Liu, D.; Zhao, Q.; Li, Q.; Zhang, J. *Adv. Mater.* **2014**, *26*, 5898−5922.
(11) Ismach, A.; Kantorovich, D.; Joselevich, E. *J. Am. Chem. Soc.* **2005**, *127*, 11554−11555.
(12) Geblinger, N.; Ismach, A.; Joselevich, E. *Nat. Nanotechnol.* **2008**, *3*, 195−200.
(13) Shadmi, N.; Geblinger, N.; Ismach, A.; Joselevich, E. *J. Phys. Chem. C* **2014**, *118*, 14044−14050.
(14) Shadmi, N.; Kremen, A.; Frenkel, Y.; Lapin, Z. J.; Machado, L. D.; Legoas, S. B.; Bitton, O.; Rechav, K.; Popovitz-Biro, R.; Galvão, D. S.; Jorio, A.; Novotny, L.; Kalisky, B.; Joselevich, E. *Nano Lett.* **2016**, *16*, 2152−2158.
(15) Soares, J. S.; et al. *Nano Lett.* **2010**, *10*, 5043−5048.
(16) Jeon, S.; Lee, C.; Tang, J.; Hone, J.; Nuckolls, C. *Nano Res.* **2008**, *1*, 427−433.
(17) Huang, J.; Choi, W. *Nanotechnology* **2008**, *19*, 505601.
(18) Yao, Y.; Dai, X.; Feng, C.; Zhang, J.; Liang, X.; Ding, L.; Choi, W.; Choi, J.-Y.; Kim, J. M.; Liu, Z. *Adv. Mater.* **2009**, *21*, 4158−4162.
(19) Yakobson, B. I.; Brabec, C.; Bernholc, J. *Phys. Rev. Lett.* **1996**, *76*, 2511.
(20) Ozaki, T.; Iwasa, Y.; Mitani, T. *Phys. Rev. Lett.* **2000**, *84*, 1712.
(21) Machado, L.; Legoas, S.; Soares, J. d. S.; Shadmi, N.; Jorio, A.; Joselevich, E.; Galvao, D. *Phys. Rev. Lett.* **2013**, *110*, 105502.
(22) Pantano, A.; Parks, D. M.; Boyce, M. C. *J. Mech. Phys. Solids* **2004**, *52*, 789−821.
(23) Tserpes, K.; Papanikos, P. *Composites, Part B* **2005**, *36*, 468−477.
(24) Arroyo, M.; Belytschko, T. *Int. J. Numer. Meth. Eng.* **2004**, *59*, 419−456.
(25) Buehler, M. J. *J. Mater. Res.* **2006**, *21*, 2855−2869.
(26) Kirchhoff, G. *J. Reine Angew. Math* **1859**, *1859* (56), 285−313.
(27) Fakhri, N.; Tsyboulski, D. A.; Cognet, L.; Weisman, R. B.; Pasquali, M. *Proc. Natl. Acad. Sci. U. S. A.* **2009**, *106*, 14219−14223.
(28) Li, C.; Chou, T.-W. *Int. J. Solids Struct.* **2003**, *40*, 2487−2499.
(29) Zhao, J.; Lu, L.; Rabczuk, T. *J. Chem. Phys.* **2014**, *140*, 204704.
(30) Bergou, M.; Audoly, B.; Vouga, E.; Wardetzky, M.; Grinspun, E. *ACM Trans. Graph.* **2010**, *29*, 116.
(31) Habibi, M.; Najafi, J.; Ribe, N. M. *Phys. Rev. E* **2011**, *84*, 016219.
(32) Jawed, M. K.; Da, F.; Joo, J.; Grinspun, E.; Reis, P. M. *Proc. Natl. Acad. Sci. U. S. A.* **2014**, *111*, 14663−14668.
(33) Jawed, M. K.; Reis, P. M. *Extreme Mech. Lett.* **2014**, *1*, 76−82.
(34) Jawed, M. K.; Brun, P.-T.; Reis, P. M. *J. Appl. Mech.* **2015**, *82*, 121007.
(35) Chiu-Webster, S.; Lister, J. *J. Fluid Mech.* **2006**, *569*, 89−111.
(36) Passieux, R.; Guthrie, L.; Rad, S. H.; Lévesque, M.; Therriault, D.; Gosselin, F. P. *Adv. Mater.* **2015**, *27*, 3676.
(37) Hearle, J.; Sultan, M.; Govender, S. *J. Text. Inst.* **1976**, *67*, 373−376.

DOI: 10.1021/acs.nanolett.7b04676
Nano Lett. 2018, 18, 1660−1667

(38) *Numerical simulation source code for elastic sewing machine.* http://www.cs.columbia.edu/cg/elastic_coiling/.
(39) Zhao, J.; Jiang, J.-W.; Jia, Y.; Guo, W.; Rabczuk, T. *Carbon* **2013**, *57*, 108−119.
(40) Shen, C. *Rarefied gas dynamics: fundamentals, simulations and micro flows*; Springer: Berlin, 2006.
(41) Heineman, M. *Comm. Pure Appl. Math* **1948**, *1*, 259−273.
(42) Rafiee, R.; Moghadam, R. M. *Composites, Part B* **2014**, *56*, 435−449.
(43) Collins, P. G.; Avouris, P. *Sci. Am.* **2000**, *283*, 62−69.
(44) Kudin, K. N.; Scuseria, G. E.; Yakobson, B. I. *Phys. Rev. B: Condens. Matter Mater. Phys.* **2001**, *64*, 235406.
(45) Yakobson, B. I.; Couchman, L. S. *J. Nanopart. Res.* **2006**, *8*, 105−110.
(46) Chang, T.; Gao, H. *J. Mech. Phys. Solids* **2003**, *51*, 1059−1074.
(47) Shokrieh, M.; Rafiee, R. *Mech. Compos. Mater.* **2010**, *46*, 155−172.
(48) Pantano, A.; Boyce, M. C.; Parks, D. M. *J. Eng. Mater. Technol.* **2004**, *126*, 279−284.
(49) Bergou, M.; Wardetzky, M.; Robinson, S.; Audoly, B.; Grinspun, E. *ACM Trans. Graph.* **2008**, *27*, 63.
(50) Brun, P.-T.; Audoly, B.; Ribe, N. M.; Eaves, T. S.; Lister, J. R. *Phys. Rev. Lett.* **2015**, *114*, 174501.
(51) Huang, J.; Wang, B.; Lahiri, I.; Gupta, A. K.; Eklund, P. C.; Choi, W. *Adv. Funct. Mater.* **2010**, *20*, 4388−4393.
(52) Brun, P.-T.; Audoly, B.; Ribe, N. M.; Eaves, T. S.; Lister, J. R. *Phys. Rev. Lett.* **2015**, *114*, 174501.

DOI: 10.1021/acs.nanolett.7b04676
Nano Lett. 2018, 18, 1660−1667